EUROPEAN ORGANIZATION FOR NUCLEAR RESEARCH

CERN-EP/90-52
23 April 1990

Measurement of the Transverse Momentum Distributions of W and Z Bosons at the CERN $\bar{p}p$ Collider

The UA2 Collaboration

Bern - Cambridge - CERN - Heidelberg - Milano
Orsay(LAL) - Pavia - Perugia - Pisa - Saclay(CEN)

J.Alitti[10], R.Ansari[6], R.E.Ansorge[2],D.Autiero[9] P.Bagnaia[3,a], P.Bareyre[10], G.Blaylock[3], P.Bonamy[10], M.Bonesini[5,3], C.N.Booth[3], K.Borer[1], D.Buskulic[6], G.Carboni[9], D.Cavalli[5], V.Cavasinni[9], P.Cenci[8], J.C.Chollet[6], C.Conta[7], G.Costa[5], F.Costantini[9,3], A.Dell'Acqua[7], B.DeLotto[7,b], T.DelPrete[9], R.S.DeWolf[2], L.DiLella[3], G.F.Egan[3,c], K.F.Einsweiler[3], L.Fayard[6], A.Federspiel[1], R.Ferrari[7], M.Fraternali[7,d], D.Froidevaux[6], G.Fumagalli[3,7], J.M.Gaillard[6], F.Gianotti[5], O.Gildemeister[3], C.Gössling[3,e], V.G.Goggi[7,3], S.Grünendahl[4], K.Hara[1,f], S.Hellman[3], E.Hugentobler[1], K.Hultqvist[3], E.Iacopini[9,g], J.Incandela[3], K.Jakobs[3], P.Jenni[3], E.E.Kluge[4], N.Kurz[4], S. Lami[4,9], P.Lariccia[8], M.Lefebvre[2,3], L.Linssen[3], M.Livan[7,h], P.Lubrano[3], C.Magneville[10], L.Mandelli[5], L.Mapelli[3], M.Mazzanti[5], K.Meier[3], B.Merkel[6], J.P.Meyer[10], M.Moniez[6], R.Moning[1], M.Morganti[9,i], L.Müller[1], D.J.Munday[2], C.Onions[3], T.Pal[3,1], M.A.Parker[3], G.Parrour[6], F.Pastore[7], E.Pennacchio[7], J.M.Pentney[2], M.Pepe[8], L.Perini[5,d], C.Petridou[9], P.Petroff[6], H.Plothow-Besch[4], G.Polesello[5,3], A.Poppleton[3], M.Primavera[9,j], L.Rasmussen[3], J.P.Repellin[6], A.Rimoldi[7], P.Scampoli[8], J.Schacher[1], S.L.Singh[2], S.Stapnes[3], A.V.Stirling[10], S.N.Tovey[3,c], M.Valdata-Nappi[9,j], V.Vercesi[3,7], A.R.Weidberg[3], P.S.Wells[2], T.O.White[2], D.R.Wood[3], S.A.Wotton[2], H.Zaccone[10]

(Submitted to Zeitschrift für Physik C)

Abstract

The transverse momentum distributions of W and Z bosons produced in $\bar{p}p$ collisions at $\sqrt{s} = 630$ GeV are examined. Comparisons are made with QCD predictions, and good agreement is found. The fraction of W bosons produced with $p_T > 25$ GeV is found to be $3.8 \pm 0.6(stat)\ ^{+0.9}_{-1.3}(syst)\%$.

1. Laboratorium für Hochenergiephysik, Universität Bern, Sidlerstraße 5, 3012 Bern, Switzerland
2. Cavendish Laboratory, University of Cambridge, Cambridge, CB3 0HE, UK
3. CERN, 1211 Geneva 23, Switzerland
4. Institut für Hochenergiephysik der Universität Heidelberg, Schröderstraße 90, 6900 Heidelberg, FRG
5. Dipartimento di Fisica dell'Università di Milano and Sezione INFN Milano, 20133 Milano, Italy
6. Laboratoire de l'Accélérateur Linéaire, Université de Paris-Sud, 91405 Orsay, France
7. Dipartimento di Fisica Nucleare e Teorica, Università di Pavia and INFN, Sezione di Pavia, Via Bassi 6, 27100 Pavia, Italy
8. Dipartimento di Fisica dell'Università di Perugia and INFN, Sezione di Perugia, via Pascoli, 6100 Perugia, Italy
9. Dipartimento di Fisica dell'Università di Pisa and INFN, Sezione di Pisa, Via Livornese, S.Piero a Grado, 56100 Pisa, Italy
10. Centre d'Etudes Nucléaires de Saclay, 91191 Gif-sur-Yvette Cedex, France

a) Now at Dipartimento di Fisica, Università di Roma, Italy

b) Now at Dipartimento di Fisica, Università di Udine, Italy

c) Visitor from the University of Melbourne, Parkville, Australia 3052

d) Now at Istituto di Fisica, Università di Palermo, Italy

e) Now at Institut für Physik, Universität Dortmund, FRG

f) Now at University of Tsukuba, Tsukuba, Ibaraki 305, Japan

g) Also at Scuola Normale Superiore, Pisa, Italy

h) Now at Dipartimento di Fisica, Università di Cagliari, Italy

i) Now at Dipartimento di Fisica e INFN, Sezione di Bologna, Università di Bologna, Italy

j) Now at Dipartimento di Fisica dell'Università della Calabria e gruppo INFN, Cosenza, Italy

1 Introduction

Intermediate Vector Bosons (IVB's) produced in proton-antiproton collisions are often accompanied by initial state gluon radiation which provides transverse momentum to the IVB. Two approaches have traditionally been used to study the IVB production cross section as a function of the transverse momentum (p_T^{IVB}). In the first approach, exclusive tree level perturbation calculations [1] have been compared with data [2] for specific topologies of IVB+jet(s) events. Unfortunately, these predictions suffer from corrections for terms beyond the tree level which have not been calculated, and also from sensitivity to the jet definition. In the second approach, the inclusive spectrum is examined [3]. At low values of p_T^{IVB} where multiple soft gluon emission is expected to dominate the initial state radiation, the IVB production cross section is calculated using soft gluon resummation techniques [4]. In the high-p_T regime ($p_T^{IVB} \gtrsim 20$ GeV), the cross section is expected to be well described by QCD perturbation theory [4], and complete $O(\alpha_s^2)$ calculations are now available for this case [5,6].

In the following analysis, the inclusive spectra of p_T^Z and p_T^W are examined. These distributions are measured by the UA2 experiment from the electronic decay modes of the bosons, $Z \rightarrow e^+e^-$ and $W \rightarrow e\nu$. These measurements are of interest for several reasons. Firstly, the p_T dependence of the IVB cross sections provides a more sensitive test of QCD than the total cross section. Equally importantly, one can look for deviations from the theoretical predictions which might indicate physics beyond the Standard Model. This is especially true for large values of $p_T^{IVB}$where the events are characterized by jet(s) plus leptons and/or missing transverse energy. These are typical signatures in the searches for new physics processes such as heavy quark production or supersymmetry. Finally, good understanding of the p_T^W measurement, as well as the intrinsic p_T^W distribution, is essential for a precise determination of the W mass [7].

2 The UA2 Apparatus

The UA2 detector was substantially upgraded between 1985 and 1987. Reference [8] contains a summary of the features of the apparatus relevant to the study of W and Z bosons, and only the major points are repeated here. Additional details about specific detector elements can be found in the references given below.

A quadrant of the detector is shown in Fig. 1. The pseudorapidity (η) coverage of the central calorimeter [9] of $-1 < \eta < 1$ has been extended with new end cap calorimeters to $-3 < \eta < 3$ [10]. The same technique (lead and iron absorber plates with scintillator and wavelength shifter readout) is used throughout. An electromagnetic compartment with lead absorber plates of 17.0-24.4 radiation lengths (depending on polar angle) is followed by hadronic compartments with iron absorber plates. In the central calorimeter, the hadronic region is subdivided in depth into two compartments of two interaction lengths each. The lateral segmentation in the central calorimeter is constant in azimuth and polar angle ($\Delta\phi = 15°$, $\Delta\theta = 10°$). In the end caps, the two cells closest to the beam axis ($2.5 < |\eta| < 3.0$ and $2.2 < |\eta| < 2.5$) cover 30° in azimuth, and the other cells have a

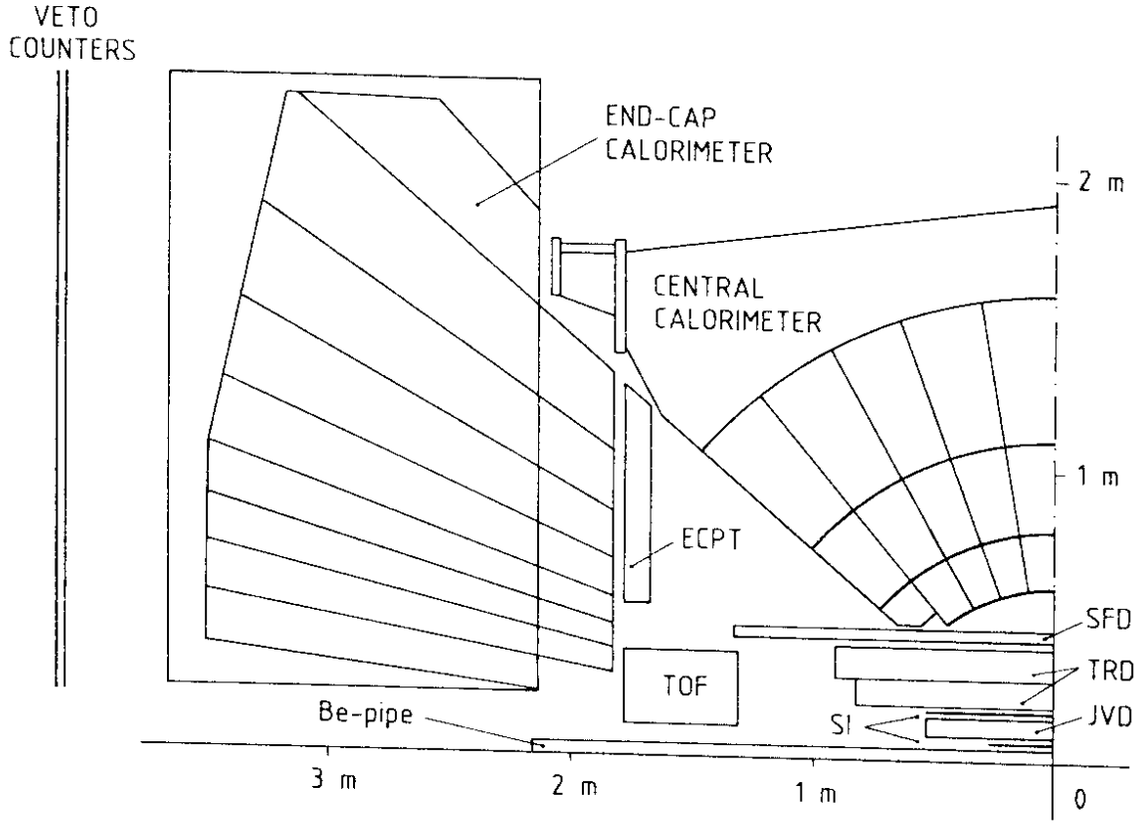

Figure 1: A schematic view of one quadrant of the UA2 detector.

constant segmentation $\Delta\phi = 15°$, $\Delta\eta = 0.2$.

Clusters are constructed in the calorimeter by joining all cells with an energy greater than 400 MeV sharing a common edge. Those clusters with a small lateral size and a small energy leakage into the hadronic compartments are marked as electromagnetic clusters and are subsequently examined as potential electron candidates.

The response of the calorimeter to hadronic showers depends on the fraction of the energy carried by photons. An average correction factor, determined from pion test beam data, is defined for each compartment of the calorimeter. These weights are used to multiply the observed energies in hadronic showers in order to compensate for the difference from electron showers. The weights applied to the electromagnetic cells are 1.18 in the central calorimeter and 1.20 in the end caps. In addition, a factor of 1.06 is applied to the second hadronic compartment in the central calorimeter to account for energy leaking through the back of the calorimeter.

The layout of the central detector is included in Fig. 1. Around the beam pipe, at radii of 3.5 cm (inner) and 14.5 cm (outer), are two arrays of silicon counters used for tracking and ionization measurements [11]. Between the two is a cylindrical drift chamber with jet geometry (the Jet Vertex Detector or JVD) [12]. Outside of the inner tracking detectors is the Transition Radiation Detector (TRD) [13], consisting of two sets of radiators and proportional chambers. The outermost of the central detectors is the Scintillating Fibre Detector (SFD) [14], which consists of approximately 60 000 fibres arranged on cylinders into 8 stereo triplets.

The last elements before the calorimeters are "preshower detectors", used to localize the early development of electromagnetic shower initiated in a lead converter. In front of the central calorimeter, this function is served by the SFD, where 1.5 radiation lengths of lead are positioned before the last two stereo triplets of fibres. For the end cap region, the preshower detection is accomplished by the End Cap Proportional Tubes (ECPT) [15], which consist of a stereo triplet of proportional tubes behind a 2 radiation length lead converter. Two stereo triplets in front of the converter act as tracking chambers. In each case, an electron is identified by a large cluster of charge in the preshower region (after the converter) which lies close to a reconstructed track [8].

3 Event Sample

The data were collected from 1988 to 1989 at the CERN $\bar{p}p$ collider at an energy of $\sqrt{s} = 630$ GeV. Over this period, the UA2 experiment accumulated 7.8 pb^{-1} of integrated luminosity. After removing events where not all of the detector elements used in this analysis were functioning, the useful integrated luminosity is 7.4 ± 0.4 pb^{-1}. Requirements are imposed in order to select events where $\bar{p}p \rightarrow W+X$, $W \rightarrow e\nu$ or $\bar{p}p \rightarrow Z+X$, $Z \rightarrow e^+e^-$. Apart from the few exceptions noted below, the samples obtained are identical to those used in the measurement of the W and Z production cross sections [8], so most details are omitted in the following description of the selection.

3.1 Electron Identification

A standard electron candidate must have a track reconstructed in the tracking detectors which points to an electromagnetic cluster in the calorimeter. The track must originate from a reconstructed vertex which is not displaced more than 250 mm along the beam direction from the center of the detector. The lateral and longitudinal profile of the shower in the calorimeter is required to be consistent with that expected from an electron incident along the track trajectory. Furthermore, a preshower cluster must be reconstructed which is consistent with the position of the electron candidate track.

In addition, a set of looser electron cuts is defined for the region covered by the central calorimeter, in order to recover electrons for which either the track or the preshower cluster is not correctly reconstructed by the standard pattern recognition algorithms. In such cases, SFD data from the vicinity of the electron candidate are examined, and cuts are made directly on the number of layers hit in the tracking region or on the charge detected in the preshower layers [8].

The detected energy is summed in a small number (typically two) of calorimeter cells which are assigned to the electron. Energy corrections are applied according to the precise electron direction and impact point in the calorimeter based on data obtained from 40 GeV test beam electrons. The corrected energy is used together with the direction given by the tracking detectors to define $\vec{p}^{\,e}$, the electron momentum.

3.2 Neutrino Identification

The presence of neutrinos in $W \rightarrow e\nu$ decays is deduced by measuring the electron energy and the energies of the particles (generally hadrons) recoiling against the W. The missing transverse momentum ($\not\!\!p_T$) is attributed to the undetected neutrino:

$$\vec{p}_T^{\,\nu} \simeq \vec{\not\!\!p}_T = -\vec{p}_T^{\,e} - \vec{p}_T^{\,rec}. \tag{1}$$

Here, $\vec{p}_T^{\,e}$ is the reconstructed transverse momentum of the electron candidate and $\vec{p}_T^{\,rec}$ is the total transverse momentum of the recoil particles, calculated as

$$\vec{p}_T^{\,rec} = \left(\sum E_{cell}\hat{v}_{cell}\right)_T, \tag{2}$$

where $\hat{v}_{cell}$ is a unit vector from the interaction vertex to the center of a calorimeter cell, E_{cell} is the weighted sum of compartment energies in that cell, and the sum extends over all cells in the calorimeter ($-3 < \eta < 3$) excluding the cells assigned to the electron.

3.3 Z Selection Requirements

Z events are required to contain two electron candidates detected in the combined fiducial volume of the calorimeters and preshower detectors ($|\eta| \lesssim 1.6$). At least one of the two must satisfy the standard electron cuts while the other is allowed to satisfy either the standard or the looser cuts. The invariant mass of the electron candidate pair (m_{ee}) is calculated from the corrected momenta of the electrons. Those events with m_{ee} between 76 and 110 GeV are chosen as Z candidates. This leaves a sample of 162 events. A QCD background of 2.4 events in this sample is estimated by studying the populations of the Z signal region and a background region ($40 < m_{ee} < 70$ GeV) when the electron identification cuts are relaxed for one or both electron candidates [8]. Seven events of the type $Z \rightarrow ee\gamma$, which appear in the cross section sample [8], are not included in this study.

A feature of the Z trigger is to require two quartets of adjacent calorimeter cells (2×2), each with transverse energy measured in the electromagnetic compartments exceeding 5 GeV and separated in azimuth by at least 60°. For events with p_T^Z up to $\approx$ 50 GeV, however, this requirement introduces no significant inefficiency.

3.4 W Selection Requirements

W candidates must have an electron inside the fiducial volume of the central calorimeter ($|\eta| < 0.97$) which passes standard cuts and has transverse momentum greater than 20 GeV. The neutrino transverse momentum reconstructed in each event must exceed 20 GeV. The transverse mass, m_T, is required to be greater than 40 GeV, where $m_T \equiv \sqrt{2p_T^e p_T^\nu(1 - cos\phi^{e\nu})}$ and $\phi^{e\nu}$ is the azimuthal separation between the measured electron and neutrino directions. This leaves 1676 events. A contribution of about 3.8% is expected from τ events ($W \rightarrow \tau\nu$, $\tau \rightarrow e\nu\nu$), but these events produce a correctly measured p_T^W and are therefore an acceptable signal for this analysis.

The total QCD background remaining in this sample is less than 1%, as determined from a separate analysis [8]. Although this is a small fraction, it is important to understand

the shape of the background as a function of p_T^W. Even a small background could distort the spectrum if it were concentrated at high p_T where the signal is falling rapidly. Indeed, QCD background tends to come from mismeasured two-jet events in which one jet is misidentified as an electron and the second jet is interpreted as a high p_T system recoiling against the fake W.

The QCD background is studied with a special data sample, corresponding to 2.8 pb^{-1}, which was not subjected to a $\not\!\!p_T$ requirement in the trigger. Events are selected from this sample with the standard electron identification requirements and a cut of $p_T^e > 20$ GeV. A distribution of m_T *vs.* p_T^W, shown in Fig. 2(a), is constructed from the remaining events. The region where $m_T < 30$ GeV ("background region") is dominated by jet events with a jet misidentified as an electron. On the other hand, the region where $50 < m_T < 90$ GeV and $p_T^W < 10$ GeV ("signal region") is dominated by real W events. When the electron identification cuts are tightened (by requiring a tighter match between the track and the preshower cluster and asking for a better quality electron signal in the calorimeter) relative factors for rejection of QCD jets and efficiency for electrons are measured from the two regions. With the same tight cuts applied to the standard W sample, the efficiency and rejection are used to determine the amount of background present in each range of p_T^W. The result is shown in Fig. 2(b), indicating that the background does not accumulate at high p_T^W. It remains less than 10% even for $p_T^W > 20$ GeV. The two-jet events which mimic high p_T W's tend to have low transverse mass and are effectively eliminated by the m_T cut.

4 Physics and Detector Models

For the inclusive measurement considered here, a theoretical model consists of a differential distribution in rapidity and transverse momentum (y, p_T). At lower values of p_T^{IVB} ($\lesssim 30$ GeV) these distributions are taken from the soft gluon resummation calculations of Altarelli *et al.* [4]. For larger values of p_T^{IVB}, the complete $O(\alpha_s^2)$ calculation of Arnold and Reno [5] is used.

In each case, aside from the calculation, one must choose a set of structure functions, a value for Λ_{QCD}, and a scale to use for the running coupling constant and the parton densities. In most cases, the scale $Q^2 = M_{IVB}^2$ is chosen, and DFLM [16] structure functions are used. The exception is the high p_T^{IVB} prediction of Bawa and Stirling [17], which applies the formulae of Arnold and Reno at an optimized scale $Q^2 = (0.5 p_T^{IVB})^2$ and uses MRSB′ structure functions [18].

In order to go from a theoretical (y, p_T) distribution to a prediction that can be compared with a measured spectrum, a simple Monte Carlo simulation is used. For each theoretical model, the simulation generates W or Z bosons according to the appropriate (y, p_T) distribution, forces them to decay into leptons, and models the detector response. Each electron is followed into the calorimeter and smearing is applied to the energy and direction to account for the measurement errors. The energy resolution, which depends on the impact point and cell type, is obtained from look-up tables based on test beam data (the electron response model is described in detail in Ref. [7]). The hadrons in the event

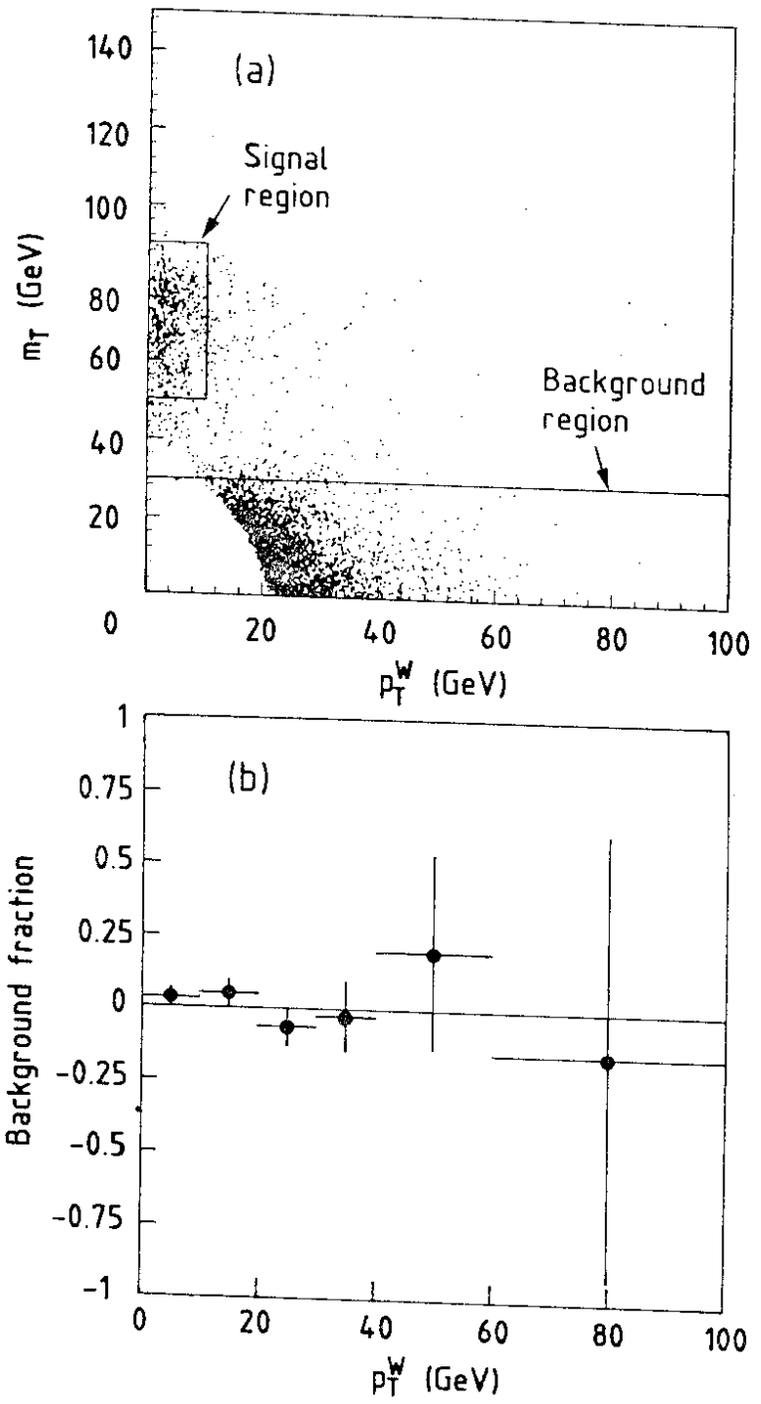

Figure 2: (a) The signal and background regions used to determine the relative efficiency and rejection of the electron identification cuts. (b) The estimate of the QCD background fraction as a function of p_T^W.

are modeled globally, with no individual treatment of hadrons or jets. The model produces, as a function of p_T^{IVB}, an observed p_T^{rec}, the total measured p_T of the recoiling underlying event. This part of the model is essential to the understanding of the p_T^W measurement and it is described in greater detail in section 6.1.

5 p_T^Z Measurement

The transverse momentum of Z bosons (p_T^Z) is evaluated from p_T^{ee}, the measured total transverse momentum of the two decay electrons. The p_T^Z spectrum is shown in Fig. 3(a). The measurement errors on p_T^{ee} are dominated by the energy resolution of the calorimeter, and are estimated to be about 2 GeV. The mean corresponding to the distribution shown ($0 < p_T^Z < 30$ GeV) is found to be $\langle p_T^Z \rangle = 7.0 \pm 0.4 \pm 0.1$ GeV, after correcting for acceptance and resolution effects. The first error is statistical and the second corresponds to systematic uncertainties in the calorimeter resolution.

A more precise measurement can be made for the η component of p_T^{ee}, where the η direction is defined as the inner bisector of the angle between the transverse directions of the two electrons. This component is relatively insensitive to fluctuations in the electron energy measurement, relying mainly on the angles of the electrons which are well measured. A resolution of about 0.3 GeV is estimated. This distribution of p_η^Z is shown in Fig. 3(b).

In Fig. 3, the predictions of Ref. [4] are superimposed on the data. The curves have been modified to account for detector acceptance and resolution, and the predictions are normalized to the observed number of events. The principal theoretical uncertainties are due to the lack of precise knowledge of certain input parameters, namely Λ_{QCD}, the parton distribution functions, and the scale of the running coupling constant. The plausible range of variations is represented by changing the value of Λ_{QCD} used in the calculation; curves are shown for Λ_{QCD}=0.16, 0.26, 0.36 GeV (four-flavor values) where the appropriate DFLM structure functions are used in each case. The best agreement with the data, for both p_T^Z and p_η^Z, is obtained for $\Lambda_{QCD} \approx 0.26$ GeV, as determined from a maximum likelihood fit, but there is acceptable agreement over the range Λ_{QCD}=0.15-0.4 GeV (90% CL, statistical errors only). The strongest disagreement, although consistent with a statistical fluctuation, occurs at very low p_T ($\lesssim 3$ GeV), where the prediction consistently exceeds the data. The uncertainties in detector resolution introduce uncertainties equivalent to a change in Λ_{QCD} of ± 0.03 GeV (± 0.01 GeV) for p_T^Z (p_η^Z).

It must be emphasized that this should not be considered as a measurement of Λ_{QCD}. Instead, Λ_{QCD} has been treated as a parameter which reflects the theoretical uncertainties in the p_T^{IVB} calculation. In order to make a meaningful measurement of Λ_{QCD}, some important theoretical issues must be addressed. For example, the scale in the calculations is chosen somewhat arbitrarily to be $Q^2 = m_{IVB}^2$. In the leading order calculation [4], the effects of a change in Λ_{QCD} can be essentially cancelled by a shift in the scale. In order to draw more quantitative conclusions about QCD, a resummed calculation matched to the second order perturbative expression is needed, along with additional statistics in the data sample. Nonetheless, the p_T^Z data provide constraints on the p_T^{IVB} spectrum which are useful, for instance, in the analysis of the IVB masses [7].

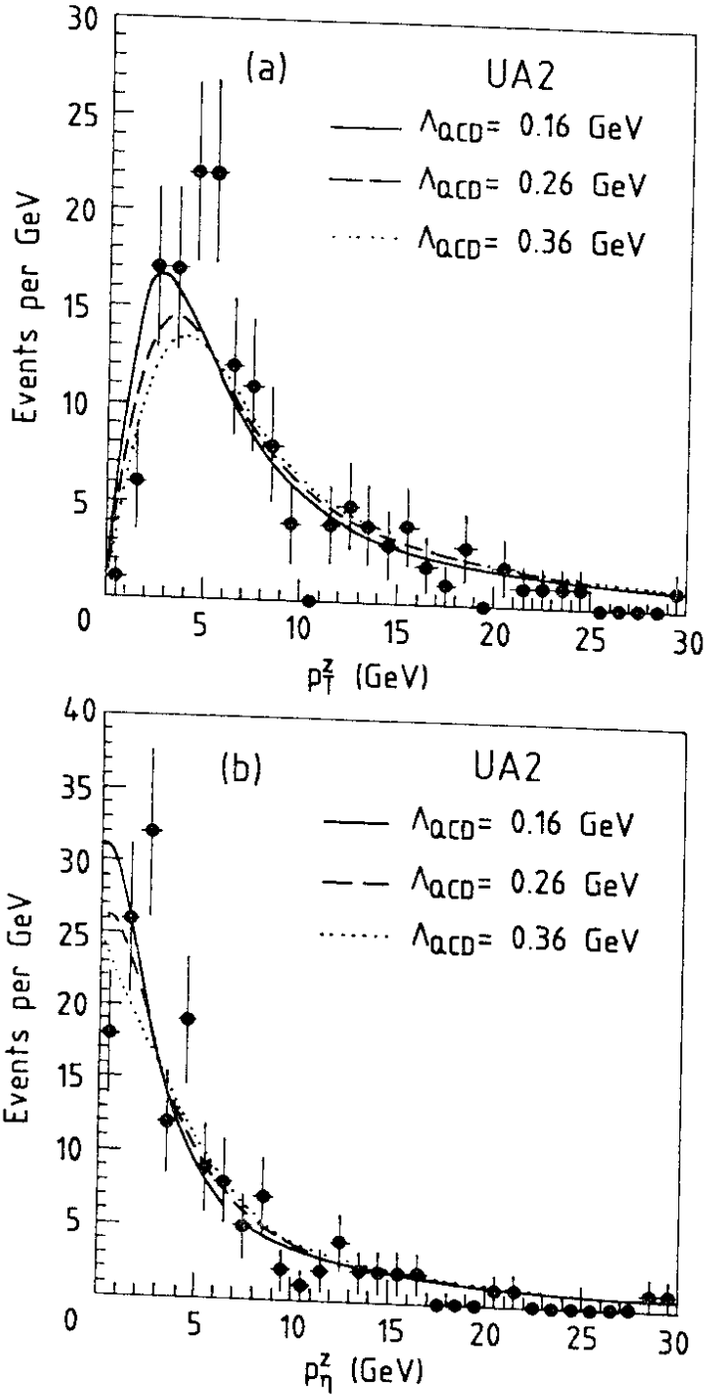

Figure 3: (a) The observed p_T^Z spectrum (points) compared with the QCD predictions of [4] for three different values of Λ_{QCD}. (b) The same comparison for the η component (see text) of p_T^Z.

6 p_T^W Measurement

6.1 Measurement Technique

The measurement of the boson momentum is more complicated for the W than for the Z. In $W \to e\nu$ decays, one measures only the electron momentum and $\vec{p}_T^{rec}$, the transverse momentum of the system of particles which recoils against the W. Transverse momentum is assumed to balance, and the missing p_T is attributed to the undetected neutrino:

$$\vec{p}_T^{\,e} + \vec{p}_T^{\,rec} + \vec{p}_T^{\,\nu} \simeq 0. \tag{3}$$

The W momentum is taken to be the sum of the electron and neutrino momenta, so p_T^W is measured only from the recoiling hadrons:

$$\vec{p}_T^{\,W} = \vec{p}_T^{\,e} + \vec{p}_T^{\,\nu} \simeq -\vec{p}_T^{\,rec}. \tag{4}$$

Recall that $\vec{p}_T^{\,rec}$ is calculated as the vector sum of p_T in all of the calorimeter cells excluding those assigned to the electron, as defined in equation (2). Similarly, the total transverse energy of the recoil system is defined by the scalar sum

$$\tilde{E}_T = \sum |(E_{cell}\hat{v}_{cell})_T|, \tag{5}$$

where the sum again excludes the cells associated with the electron.

The nature of the p_T^{rec} measurement requires careful consideration of detector resolution and systematic error. To understand these effects, it is useful to consider the recoil system as a combination of two contributions. Initial state gluon radiation recoils against the W, providing the largest contribution to the transverse momentum (there is also some contribution from the initial parton transverse momenta inside the p or $\bar{p}$, but this is small on the scale of radiative effects). At the same time, particles from spectator processes which carry a negligible total transverse momentum contribute to the resolution of the p_T^{rec} measurement, which depends mainly on $\tilde{E}_T$. In contrast, any systematic bias in the measurement of p_T^W is expected to depend primarily on p_T^W itself, since it can only result from some mismeasurement of the initial state radiation which produces the transverse momentum.

To understand the resolution effects, studies are made of two different event samples, taken from minimum bias triggers and two-jet triggers, which are expected to bound the resolution for W events. Minimum bias and two-jet events do not, in general, contain significant physics sources of $\not\!\!p_T$ such as energetic neutrinos. Consequently, the observed $\not\!\!p_T$ in these events provides a measure of the momentum resolution of the detector. The two orthogonal transverse momentum components have nearly Gaussian distributions, leading to the following formula:

$$\frac{dN}{d\not\!\!p_T{}^2} \propto \exp\left(\frac{-\not\!\!p_T{}^2}{\Delta^2}\right). \tag{6}$$

The resolution parameter Δ is measured for different ranges of $\tilde{E}_T$, and is parameterized for minimum bias data as shown by the open circles in Fig. 4. Two-jet triggers, on the other

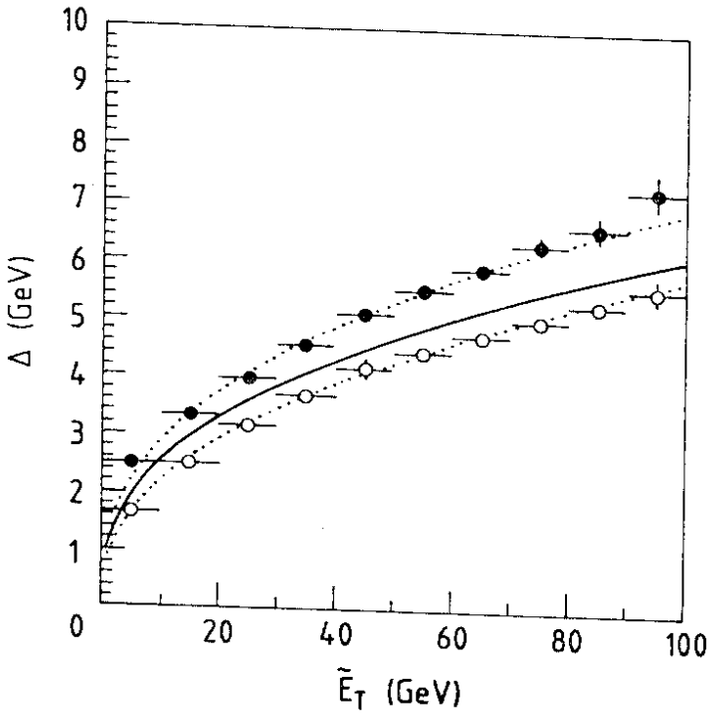

Figure 4: The missing momentum resolution as a function of $\tilde{E}_T$. The upper dotted curve is derived from two-jet data, while the lower dotted curve comes from minimum bias triggers. The intermediate solid curve represents the best estimate used for modeling W events. The parameter Δ is defined in the text.

hand, provide examples of true recoiling underlying events. The $\not{p}_T$ resolution is measured in these events, and a subtraction is performed to account for the contribution from energy fluctuations of the two-jet system. The corrected data are shown as the solid circles in Fig. 4. In this case, $\tilde{E}_T$ represents the transverse energy of the underlying event excluding the contribution from the two jets themselves. The degraded resolution for two-jet events over minimum bias triggers is attributed to the presence of initial state radiation which changes the energy flow of the underlying event. This radiation is stronger for two-jet events than for W events due to the dominance of gluon-gluon interactions. Thus, it is reasonable to use the two-jet data as an upper limit for the p_T^W resolution. Similarly, the minimum bias data provide a natural lower limit on the p_T^W resolution.

To make use of the resolution functions shown in Fig. 4, the relation between p_T^W and $\tilde{E}_T$ is needed (recall that the inclusive theoretical models only provide a way of calculating the transverse momentum and rapidity of the W). This relation is obtained from an empirical model based on W events themselves. In practice, the Monte Carlo simulation generates p_T^W values according to one of the theoretical models. For each event, it then obtains a value of $\tilde{E}_T$ from a distribution which depends on p_T^W. These distributions are constructed to follow closely the observed distribution of $\tilde{E}_T$ *vs.* p_T^W, and in particular to reproduce the

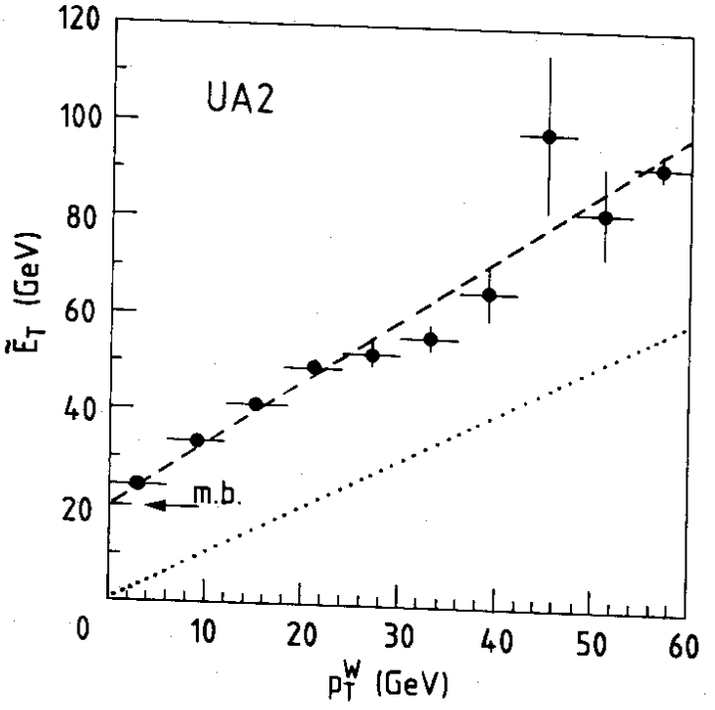

Figure 5: The average $\tilde{E}_T$ (total transverse energy observed within $|\eta| < 3$ not including the electron) as a function of p_T^W for W events. The dotted line indicates the trivial kinematic limit $p_T^W = \tilde{E}_T$, the dashed line is the parameterization of $\langle \tilde{E}_T \rangle$ vs. p_T^W used in the Monte Carlo, and the arrow shows the average value of $\tilde{E}_T$ for minimum bias events.

relation between $\langle \tilde{E}_T \rangle$ and p_T^W shown in Fig. 5. Finally, the $\tilde{E}_T$ value obtained is used to calculate a resolution for p_T^W from the parameterizations shown in Fig. 4.

There are various effects which can cause p_T^{rec} to systematically underestimate the true magnitude of p_T^W. These effects are expected to come from three sources: (1) some of the recoiling hadrons are produced at very low angles by initial state gluon radiation and therefore escape detection; (2) for slow particles, the energies measured by the calorimeter may be smaller than their momenta; and (3) calorimeter non-linearity and readout thresholds produce a small reduction in the measured p_T. At low p_T^W, where the transverse momentum is generated by the emission of multiple forward moving gluons, there is a large fractional underestimate of p_T^W primarily due to acceptance losses. At high p_T^W, there are small remaining errors due to sources (2) and (3).

The systematic effects in the p_T^{rec} measurement are examined with detailed Monte Carlo studies which include complete event generation and detailed simulation of the calorimeter. These studies provide relations between $\langle p_T^{rec} \rangle$ and p_T^W which are parameterized as shown in Fig. 6(a) and used in the detector response model in the simple Monte Carlo which is used to generate the curves in the following figures. These effects, however, are difficult to model due to their sensitivity to the detailed energy and rapidity distributions of the particles in the underlying event. Therefore, the predictions of the detailed Monte Carlo for p_T^{rec} are only qualitatively reliable. The best method for obtaining a quantitative estimate of the systematic bias is to examine $Z \rightarrow e^+e^-$ events, where the p_T of the boson can be measured directly from the e^+e^- pair and compared to the p_T^{rec} measured from the underlying event (ideally, one would expect $\vec{p}_T^{\,rec} + \vec{p}_T^{\,ee} = 0$). The measurement bias of p_T^{rec} in W and Z events should be indistinguishable due to the similarity of the production mechanism.

If one examines the momentum balance in Z events along the η direction, the contribution to the resolution from p_T^{ee} is negligible, so p_η^{ee} is a good estimate of p_η^Z. The average of $p_\eta^{ee} + p_\eta^{rec}$ is plotted as a function of p_T^{ee} in Fig. 6(b). The low statistics available for this study (162 events in total, 8 events in the region $20 < p_T^{ee} < 30$ GeV) do not allow a precise determination of the bias, but some useful restrictions are obtained, nonetheless. The uppermost dotted curve in the plot shows the direct results of the Pythia Monte Carlo [19], which clearly overestimate the bias. This curve is therefore used as an upper limit on the bias when calculating systematic errors. Although the predominantly positive sign of the data demonstrates a tendency for p_T^{rec} to underestimate the true p_T^{IVB}, the measurements are nearly consistent with no bias at all. Therefore, a lower limit on the bias is chosen which does not contain any contribution from the differences between particle momenta and energies, nor from calorimeter non-linearities or thresholds, and contains only very small acceptance losses (lowermost dotted curve in Fig. 6). The best estimate of the detector response is taken as average of these two extremes (solid curve in Fig. 6). A substantial increase in the number of observed $Z \rightarrow e^+e^-$ events would make an important improvement in the understanding of the p_T^{rec} measurement systematics.

6.2 Results

Figure 7 shows the low momentum range of the p_T^W distribution. The mean of the intrinsic distribution corresponding to this range ($0 < p_T^W < 30$ GeV) is measured to be

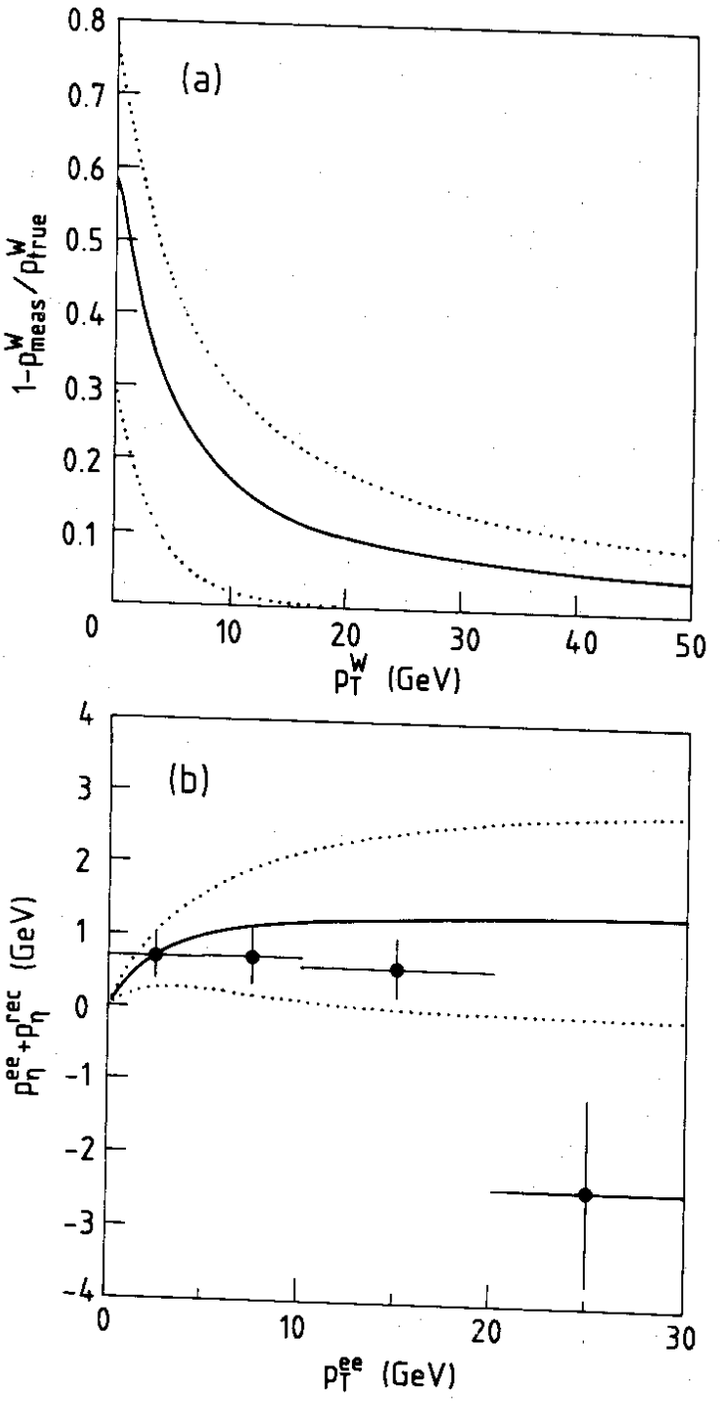

Figure 6: (a) The fractional underestimate of p_T^W due to the measurement of p_T^{rec}. (b) The momentum balance along the η direction $(p_\eta^{ee} + p_\eta^{rec})$ in $Z \to ee$ events vs. p_T^{ee}. In both figures the dotted curves show the limits established for the purposes of systematic uncertainties while the solid curves correspond to the best estimate of the detector response.

$\langle p_T^W \rangle = 6.4 \pm 0.1 \pm 0.8$ GeV, after unfolding detector acceptance and resolution. The first error is statistical and the second corresponds to variations in the corrections when the two extreme models of the detector response are adopted. As for p_T^Z, the curves represent the calculation of Ref. [4]. The consequences of the uncertainties in detector response are displayed in Fig. 7(a). Figure 7(b) shows the same data compared to theory for different values of Λ_{QCD}. The agreement is quite good, but the uncertainty in detector response precludes any quantitative conclusions.

For the high p_T tail of the distribution, the uncertainties in detector response are less important. In addition, in this region perturbative calculations are expected to be reliable and the data can be compared with the $O(\alpha_s^2)$ calculation of Ref. [5]. This comparison is shown in Fig. 8(a), where the fraction of events is shown for $p_T^W > 20$ GeV. Again, the dotted curves show the limits of detector response. As in the low momentum region, the agreement is quite good. In Fig. 8(b), we show the possible variations in the theoretical predictions by varying Λ_{QCD}, structure functions, and the Q^2 scale. The solid and dashed curves are derived from the calculations of Ref. [5] with $Q^2 = M^2$, using DFLM structure functions with values of Λ_{QCD} of 0.160 and 0.360 GeV, respectively. The dotted curve is the prediction of Ref. [17] which employs the calculation of Ref. [5] with an optimized renomalization scale of $Q^2 = (0.5 p_T^W)^2$, using MRSB′ structure functions with $\Lambda_{QCD} = 0.2$ GeV.

The first order calculation [4] yields the prediction that $5.4 \pm 2.3\%$ of the W's produced should have p_T^W above 25 GeV, while the second order calculation [5] gives a more precise estimate of $2.8 \pm 0.3\%$ for this fraction [20]. There are 52 events observed in this region. After correcting for measurement effects, a relative cross section of

$$(1/\sigma_{total})\sigma(p_T^W > 25 \text{ GeV}) = 3.8 \pm 0.6(stat) \, {}^{+0.9}_{-1.3}(syst)\% \tag{7}$$

is obtained. The systematic errors are dominated by the uncertainties in detector response applied to the steeply falling spectrum. The measurement is in good agreement with the predictions, and there is no evidence for a significant excess of events at high p_T.

The absolute cross section for W's with large p_T is obtained by including the result from the recent UA2 cross section analysis [8],

$$\sigma(\bar{p}p \rightarrow W + X)BR(W \rightarrow e\nu) = 660 \pm 15(stat) \pm 37(syst) \text{ pb}. \tag{8}$$

Together, the two results imply that $\sigma(p_T^W > 25 \text{ GeV})BR(W \rightarrow e\nu) = 25 \pm 4 \, {}^{+6}_{-9}$ pb. If the $O(\alpha_s^2)$ prediction is subtracted, the measured cross section for excess contributions beyond the standard W production is $7 \pm 4^{+8}_{-11}$ pb. This may serve as a benchmark for evaluating new physics processes which would give signals equivalent to $W \rightarrow e\nu$ decays at high transverse momentum. The predicted signal rates for the most common examples of new physics processes, however, are well below this level of sensitivity. For example, the cross section for $W \rightarrow e\nu$ decays with $p_T^W > 25$ GeV from $t\bar{t}$ production ($m_{top} = 90$ GeV) is estimated to be $0.67^{+0.05}_{-0.20}$ pb. This estimate comes from the Eurojet [21] prediction of the p_T^W distribution from top decays normalized to the cross sections of Ref. [22].

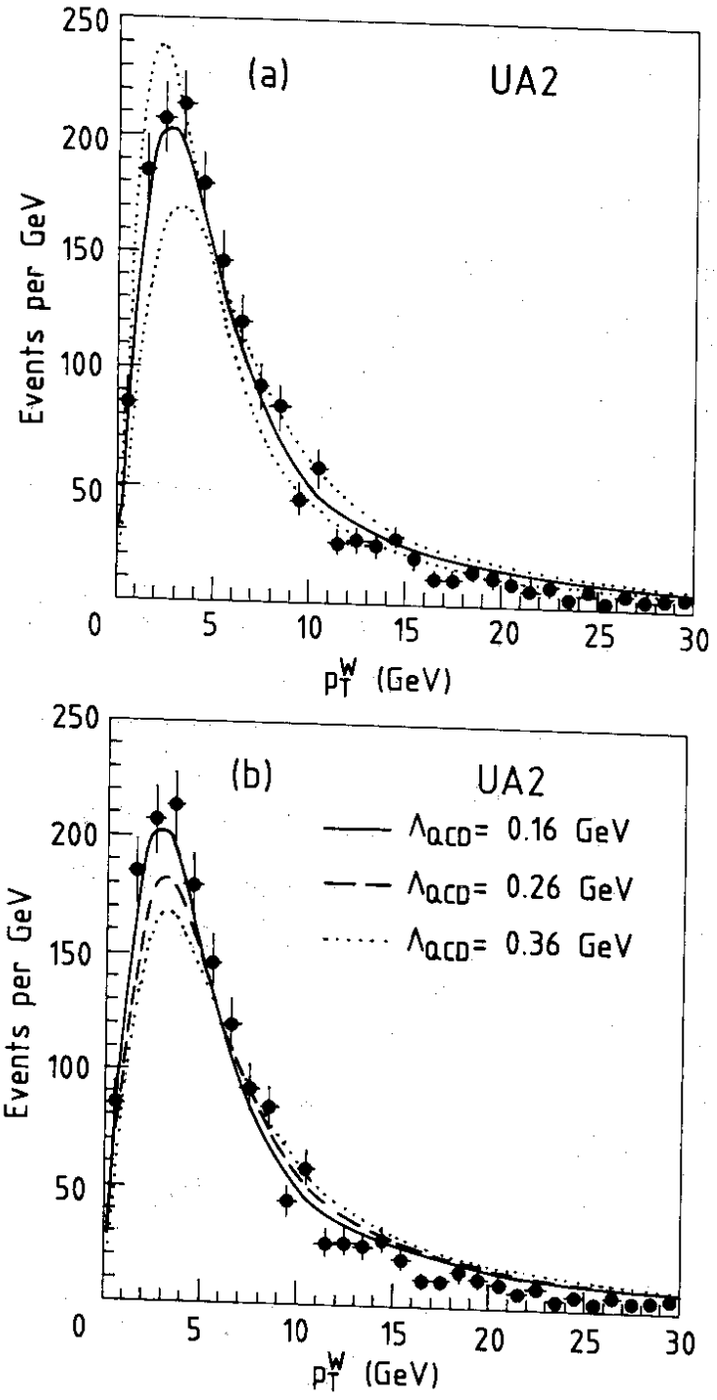

Figure 7: The observed p_T^W distribution (points) for $p_T^W < 30$ GeV. The curves show the QCD predictions of [4] (a) for Λ_{QCD}= 0.16 GeV using different models for the detector response, as described in the text, and (b) for three different values of Λ_{QCD}, using with the best estimate for the detector response.

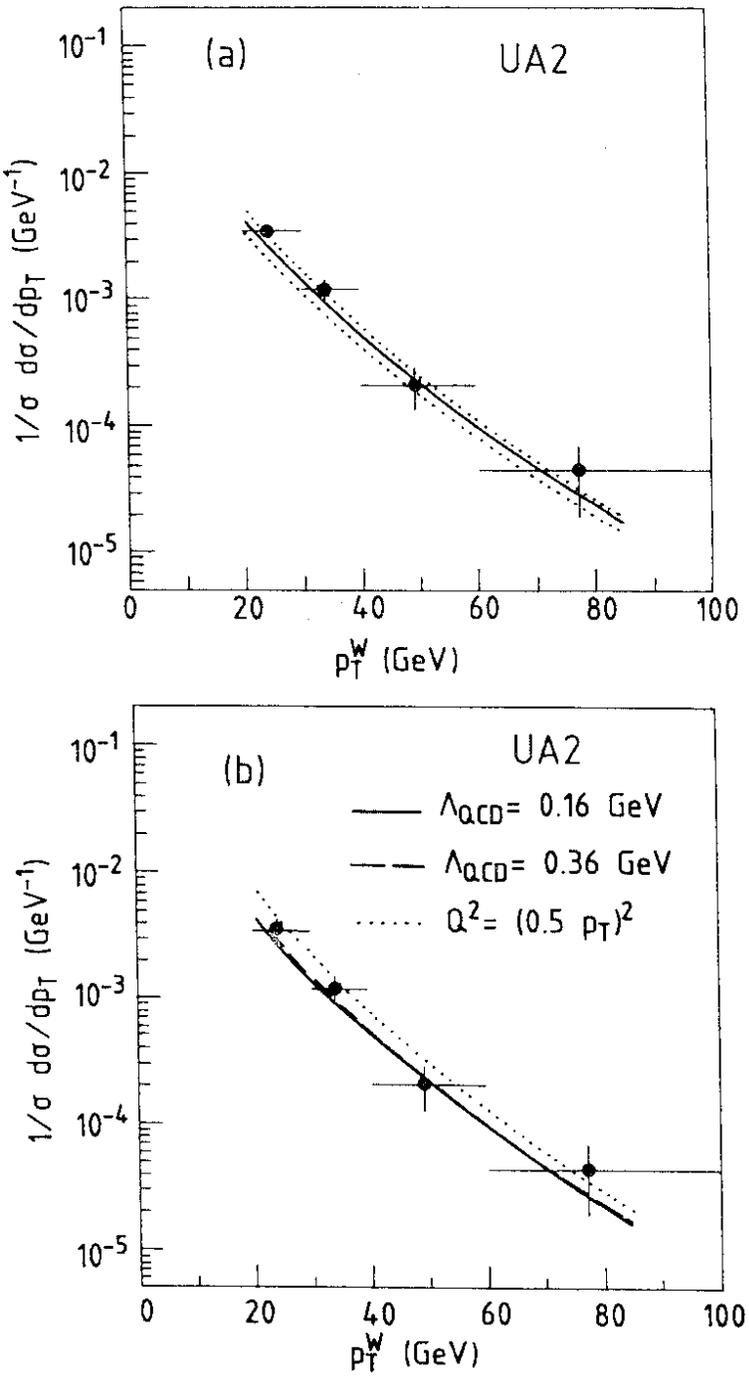

Figure 8: The observed fraction of high p_T^W events as a function of p_T^W. The curves show predictions of perturbative QCD [5] along with (a) the allowed variations in detector response and (b) including the effects of varying Λ_{QCD} and the scale Q^2.

7 Conclusions

The p_T spectra of W and Z bosons have been examined with a near tenfold increase in integrated luminosity over any previous study. For the Z, the measurement of p_T is straightforward and agrees with the predictions of leading order QCD with limited statistical precision. The measurement of p_T^W, on the other hand, requires a much more extensive understanding of detector response and consequently is more subject to systematic errors. It should be noted that a large increase in the sample of reconstructed Z decays could be used to reduce the uncertainties on the detector response to W decays, allowing much better measurements in the future. Within the systematic uncertainties, however, the p_T^W spectrum agrees quite well with predictions. It is especially interesting that the high p_T^W tail agrees with recent $O(\alpha_s^2)$ calculations, and shows no significant excess indicative of new physics processes.

Acknowledgements

Many theory colleagues have provided us with essential assistance in the form of discussions and computer programs. In particular, we would like to thank G. Altarelli, P. Arnold, A. Bawa, G. Martinelli, B. Mele, H. Reno, and J. Stirling.

We gratefully acknowledge P.Darriulat for his contributions and guidance during the design and construction of the UA2 upgrade project.

The technical staff of the institutes collaborating in UA2 have contributed substantially to the construction and operation of the experiment. We deeply thank them for their continuous support. The experiment would not have been possible without the very successful operation of the improved CERN $\bar{p}p$ Collider, whose staff and coordinators we sincerely thank for their collective effort.

Financial support from the Schweizerischen Nationalfonds zur Förderung der Wissenschaftlichen Forschung to the Bern group, from the UK Science and Engineering Research Council to the Cambridge group, from the Bundesministerium für Forschung und Technologie to the Heidelberg group, from the Institut National de Physique Nucléaire et de Physique des Particules to the Orsay group, from the Istituto Nazionale di Fisica Nucleare to the Milano, Pavia, Perugia and Pisa groups and from the Institut de Recherche Fondamentale (CEA) to the Saclay group are acknowledged.

References

[1] S.D. Ellis, R. Kleiss, W.J. Stirling: *Phys. Lett.* **B154** (1985) 435;
R. Kleiss, W.J. Stirling: *Nucl. Phys.* **B262** (1985) 235.

[2] R. Ansari *et al.* (UA2 Collaboration): *Phys. Lett.* **B215** (1988) 175.

[3] For previous measurements of the inclusive spectrum see:
J.A. Appel *et al.* (UA2 Collaboration): *Z. Phys.* **C30** (1986) 1;
C. Albajar *et al.* (UA1 Collaboration): *Phys. Lett.* **B193** (1987) 389;
R. Ansari *et al.* (UA2 Collaboration): *Phys. Lett.* **B194** (1987) 158;
C. Albajar *et al.* (UA1 Collaboration): *Z. Phys.* **C44** (1989) 15.

[4] G. Altarelli, R.K. Ellis, M. Greco, G. Martinelli: *Nucl. Phys.* **B246** (1984) 12;
G. Altarelli, R.K. Ellis, G. Martinelli: *Z. Phys.* **C27** (1985) 617.

[5] P.B. Arnold, M.H. Reno: *Nucl. Phys.* **B319** (1989) 37.

[6] R.J. Gonsalves, J. Pawłowski, C-F. Wai: *Phys. Rev.* **D40** (1989) 2245.

[7] J. Alitti *et al.* (UA2 Collaboration): CERN-EP/90-22, to appear in *Phys. Lett. B.*

[8] J. Alitti *et al.* (UA2 Collaboration): CERN-EP/90-20, to appear in *Z. Phys. C.*

[9] A.Beer *et al.*: *Nucl. Inst. and Meth.* **A224** (1984) 360.

[10] F. Alberi *et al.*: The Electron, Jet and Missing Transverse Energy Calorimetry of the Upgraded UA2 Experiment at the CERN $\overline{p}p$ Collider, in preparation for *Nucl. Inst. and Meth.*

[11] R. Ansari *et al.*: *Nucl. Instr. Meth.* **A279** (1989) 388.

[12] F. Bosi *et al.*: CERN-EP/89-82 (1989).

[13] R. Ansari *et al.*: *Nucl. Instr. Meth.* **A263** (1988) 51.

[14] R.E. Ansorge *et al.*: *Nucl. Instr. Meth.* **A265** (1988) 33;
J. Alitti *et al.*: *Nucl. Instr. Meth.* **A279** (1989) 364.

[15] K. Borer *et al.*: *Nucl. Instr. Meth.* **A286** (1990) 128.

[16] M. Diemoz, F. Ferroni, E. Longo, G. Martinelli: *Z. Phys.* **C39** (1988) 21.

[17] A.C. Bawa, W.J. Stirling: *Phys. Lett.* **B203** (1988) 172 and private communication.

[18] A.D. Martin, R.G. Roberts, and W.J. Stirling: *Phys. Lett.* **B206** (1988) 327, and *Mod. Phys. Lett.* **A4** (1989) 1135.

[19] H.-U. Bengtsson, T. Sjöstrand: *Computer Phys. Comm.* **46** (1987) 43.

[20] These values were computed using a program obtained from P. Arnold which implements the calculation of Arnold and Reno [5]. The error estimate was obtained by varying the scale between M_W^2 and ${p_T}^2$, and Λ_{QCD}(4 flavors) between 0.16 and 0.36 GeV.

[21] A. Ali, B. Van Eijk, I. ten Have: *Nucl. Phys.* **B292** (1987) 1.

[22] G. Altarelli, M. Diemoz, G. Martinelli, P. Nason: *Nucl. Phys.* **B308** (1988) 724.